Nanoscale

PAPER

Published on 06 July 2026
Licensed under CC-BY 4.0

Check for updates

Cite this: *Nanoscale*, 2026, **18**, 17276

ALD of NiO and Pt on TiO_2 nanotube arrays integrated into titanium porous transport layers for dispersion controlled electrocatalysts

Jonathan Filippi,[a] N. Calisi,[b,c] L. Capozzoli,[a] S. Caporali,[b,c] F. D'Acapito,[d] J. Orsilli,[d,e] I. Perissi,[a] C. Santoro,[d] M. Muhyuddin,[d] F. Vizza,[a] Y. Qin,[f] J. Zhang,*[f] A. Lavacchi*[a] and Enrico Berretti[a]

We present a tunable nanostructured material platform based on atomic layer deposition (ALD) of nickel oxide and platinum onto titania nanotube (TiNT) arrays embedded in a porous titanium web. The hierarchical architecture enables precise control over phase dispersion and interfacial chemistry, with NiO adopting a predominantly $Ni(OH)_2$-like local environment and co-deposited Pt stabilized as highly dispersed species. ALD cycle tuning allows systematic modulation of oxide–metal interactions, providing a versatile framework for designing low-loading noble-metal catalysts. When applied to the hydrogen evolution reaction in alkaline media, these materials show enhanced activity driven by optimized NiO_x coverage and improved Pt dispersion, achieving near-Pt performance at drastically reduced Pt loading. Tafel analysis confirms a Volmer–Heyrovsky pathway, with $Ni(OH)_2$ sites promoting proton transfer and facilitating hydrogen desorption at Pt. This work demonstrates how ALD-engineered embedded nanostructures can underpin next-generation electrocatalyst architectures.

Received 17th December 2025,
Accepted 5th June 2026

DOI: 10.1039/d5nr05314e

rsc.li/nanoscale

1. Introduction

Increasing concerns over finite fossil fuels and greenhouse gas emissions[1] are driving a global shift toward renewable energy sources.[2] However, the intermittent nature of these resources[3] creates challenges in balancing supply and demand, making efficient energy storage essential.[4] Green hydrogen, produced *via* water electrolysis powered by renewable electricity, stands out as a promising solution for large-scale, long-term storage.[5] Furthermore, green hydrogen plays a key role across multiple sectors, from transportation to steelmaking and fertilizers,[6–8] and is crucial for achieving net-zero targets.[9,10] The most established technology for green hydrogen production is alkaline electrolysis, a cost-effective approach with significant limitations, including low current densities (0.5–0.7 A cm^2), limited output pressures (<30 bar), and the need for extensive hydrogen purification.[11] Proton exchange membrane (PEM) electrolysis overcomes these limitations, offering higher current densities (up to 2 A cm^2 and above), greater efficiency, fast response times, and eliminating the need for hydrogen purification.[12,13] However, PEM electrolysis has a significant dependence on the availability of critical raw materials, relying heavily on platinum-group metals and titanium for structural components. These factors raise concerns about the sustainability of the supply chain and the overall cost-effectiveness of hydrogen production, particularly at scale.[14]

To address the challenges associated with PEM electrolysis, anion exchange membrane electrolyzers (AEMELs) have emerged as a promising alternative. They combine the advantages of both alkaline and PEM electrolysis, offering high hydrogen purity, improved efficiency, and better dynamic performance.[12] Moreover, AEMELs enable the use of more cost-effective catalysts,[15] reducing dependence on platinum-group metals and enhancing the economic viability of green hydrogen production.

Efforts to increase current density, aiming to double the current state-of-the-art performances (0.5–0.7 A cm^{-2}) in liquid alkaline systems, could reduce the stack costs, thereby significantly impacting overall system economics. Achieving this goal entails developing advanced catalysts and electrode structures

[a]*Institute of Chemistry of Organometallic Compounds (ICCOM) National Research Council (CNR), Via Madonna del Piano 10, Sesto Fiorentino, 50019, Italy. E-mail: alessandro.lavacchi@iccom.cnr.it*
[b]*Department of Industrial Engineering (DIEF) – University of Florence (UNIFI), Via di S. Marta 3, 50139 Firenze (FI), Italy*
[c]*National Interuniversity Consortium of Materials Science and Technology (INSTM), Via Giuseppe Giusti 9, 50121 Firenze (FI), Italy*
[d]*Department of Materials Science, University of Milan Bicocca, Piazza dell'Ateneo Nuovo 1, Milano 20126, Italy*
[e]*CNR-IOM Sec. Grenoble c/o ESRF-The European Synchrotron, 71 Avenue des Martyrs, CS 40220, Grenoble Cédex, 38043, France*
[f]*Interdisciplinary Research Center of Biology & Catalysis, School of Life Sciences, Northwestern Polytechnical University, Xi'an 710072, P. R. China. E-mail: zhangjiankang@nwpu.edu.cn*

This journal is © The Royal Society of Chemistry 2026

and employing highly ion-conductive membranes.[16] Electrode material selection for AEM electrolysis involves a delicate balance between factors like high electro-catalytic activity, good conductivity, corrosion resistance, and cost-effectiveness. While platinum-group materials are presently the most active and widely used electrocatalysts, their high cost and scarcity may act as a limiting factor for the large-scale deployment of green hydrogen technology.[17] However, it is worth mentioning that under alkaline conditions the hydrogen evolution reaction (HER) is significantly slower than in acidic systems. It has been reported that for Pt the rate constant for the HER is three orders of magnitude smaller than that in acidic media, but still it remains one of the most performing materials.[18] For this reason, it is crucial to find approaches that can limit Pt loading in alkaline electrodes for hydrogen evolution.

Among non-precious metal catalysts, nickel (Ni) and Ni-based alloys are known for their effectiveness in the alkaline HER. Ni is indeed widely used as a non-PGM catalyst in alkaline environments, especially in the form of metallic nickel nanoparticles or Ni-RANEY®.[19] Due to the complex nature and electrochemical behavior of nickel oxides, their electrochemical interpretation is non-trivial;[20] hence, the design of new HER electrocatalysts requires extensive electrochemical and morphological characterization. In addition, the starting surface state significantly influences the nature of the nickel deposit.[21,22] Furthermore, metallic nickel and its oxides are prone to degradation phenomena during potential cycling due to the formation of (inactive) hydrides during electrolysis and their reoxidation during shutdown or positive cycling; so the electrocatalyst state is not easily defined or controllable.[23] Furthermore, NiO-nanocluster-based electrocatalysts have been grown also on various metal substrates, allowing the observation of a synergistic effect in water splitting: the water molecule is polarized by the nickel oxide, aiding its dissociation into OH^- and H^+ and the latter is transferred to the substrate and reduced to H_2 (a Heyrovsky-type mechanism), with activities up to 3–5 times higher than those of the original bare substrate; this is particularly evident on surfaces of Ni and Ti, while for metals with a strong affinity for H (*e.g.* Pt and Ir) the effect is much less evident.[24,25]

In recent years, considerable efforts have been devoted to the development of three-dimensional transition-metal-based electrocatalysts for the alkaline HER, exploiting porous and hierarchical architectures to improve catalyst accessibility, mass transport, and active-site exposure. In particular, Ni-based systems including NiMo, NiCo, and NiFe nanostructures grown on conductive foams, felts, meshes, and fibre-based supports have demonstrated promising HER performances due to the synergistic combination of high surface area and enhanced charge transport. Recent studies have also explored hybrid architectures combining transition-metal oxides or hydroxides with ultralow noble-metal loadings to improve catalyst utilisation efficiency and interfacial charge-transfer properties.[26,27] Despite these advances, achieving simultaneous control over catalyst dispersion, oxide–metal interfacial chemistry, and mass transport within mechanically robust three-dimensional electrodes remains challenging. In this context, embedded nanotube architectures fabricated directly on porous titanium substrates provide an attractive platform for integrating hierarchical transport pathways with nanoscale control of catalyst deposition.

Building on this consideration, we tried to implement a bifunctional approach by depositing NiO on titania nanotubes: our research introduces an innovative approach involving 3D structures composed of nanotube arrays embedded within a non-woven web of titanium fibers, a concept we term "embedded nanostructure".[28] The nanotubes are obtained *via* the direct anodization of the titanium non-woven fibers, creating dual-scale porosity.[29,30] The primary objective is to reduce metal loading and enhance catalyst dispersion, addressing challenges in electrocatalytic processes. The dual-scale porosity is crucial in electrocatalysis, as it facilitates optimal mass transport of reactants while minimizing concentration polarization. Additionally, our nanostructures offer substantial surface areas, allowing for the deposition of numerous small, finely dispersed nanoparticles, providing a higher number of active sites for catalytic reactions. In our previous research, we explored various pathways for embedding nanocatalysts within 3D TiNTs, including the direct chemical growth of catalyst nanoparticles on nanotube surfaces, electroless methods using galvanic replacement for the deposition of ultra-thin electrocatalysts layers, and physical vapour deposition (PVD) to deposit thin catalyst layer deposition.[31]

This study explores the use of atomic layer deposition (ALD) to deposit nickel oxide nanoparticles onto selected substrates. This method offers precise control over particle size, loading and distribution by varying deposition parameters such as pulse time and ALD cycles, making it an effective approach for developing both PGM-free and ultralow PGM HER electrocatalysts.[32,33]

Alongside PGM-free catalysts, we also investigate PGM-containing samples by employing ALD to deposit minimal amounts of platinum-group metals in small clusters.[34,35] Additionally, we explore the co-deposition of NiO and PGMs, assessing how nickel oxide influences the distribution of platinum-group metals within the catalyst structure (Fig. 1).

2. Experimental section

2.1 Electrocatalyst preparation

The catalysts were synthesized by ALD in a homemade hot-wall reactor using ultra-high purity N_2 as the carrier gas. For the NiO catalysts, the bis(cyclopentadienyl)nickel(II) ($NiCp_2$) and O_3 were used as NiO precursor and reacting gas, respectively. The loadings were controlled by adjusting the NiO ALD cycles. The pulse, exposure and purge times for $NiCp_2$ were 4, 8, and 30 s, respectively, and the corresponding times for O_3 were 0.4, 9 and 25 s, respectively. $NiCp_2$ stored in a stainless steel bubbler was set at 68 °C, and the deposition temperature was set at 250 °C. Similarly, the Pt ALD process was performed at 250 °C with $MeCpPtMe_3$ as the Pt precursor (Strem Chemicals,

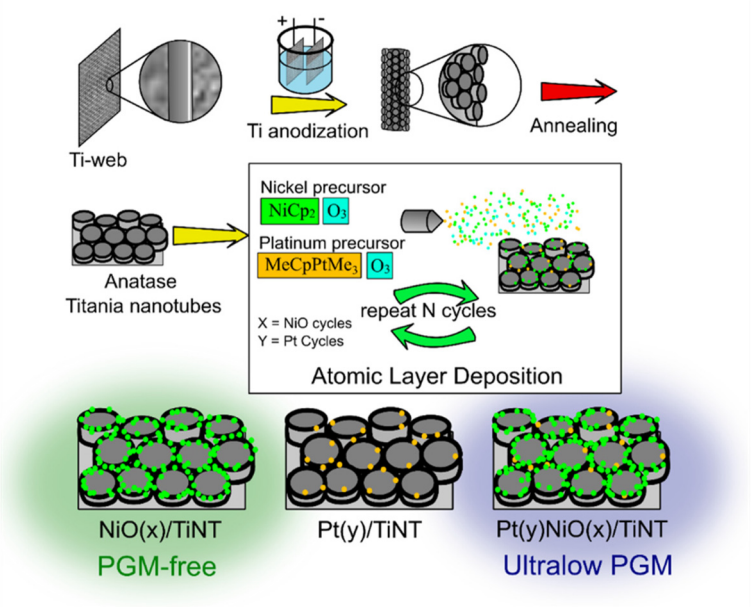


Fig. 1 Concept of the ALD-based synthesis of the electrocatalyst on titania nanotube supports.

99%) reacting with O_3 generated by an ozone generator (CH-ZTW7G-2, Guangzhou Chuanghuan Ozone Electrical Equipment Co., Ltd). $MeCpPtMe_3$ contained in the stainless steel bubbler was maintained at 60 °C to provide enough vapor pressure. The pulse, exposure and purge times for $MeCpPtMe_3$ were 0.4, 20 and 30 s, respectively, whereas those for O_3 were 0.4, 9 and 25 s, respectively. Ultra-high-purity N_2 (99.999%) was used as the carrier and purge gases at a flow rate of 50 sccm and a pressure of 60 Pa. For NiO ALD, bis(cyclopentadienyl)nickel(II) ($NiCp_2$, Strem Chemicals, 98%) was used as the precursor reacting with O_3, which was maintained at 68 °C to provide enough vapor pressure.

2.2 SEM and TEM characterization

Scanning electron microscopy characterization was performed using a Tescan Gaia 3 FIB/SEM microscope. Images were collected in beam deceleration mode with a landing energy of 5 kV, using the in-beam detectors.

HR-TEM (high resolution transmission electron microscopy), STEM (scanning transmission electron microscopy) and EDS characterization studies were performed using a Thermo Fisher TALOS F200X G2 TEM, equipped with an in-built four-segment annular EDX detector. Characterization was performed by exploiting an electron beam of 200 kV energy. Elemental quantification was performed on oxide flakes detached from the surface after a sonication/drop casting procedure on mesh portions. All the samples comprised only TiO_2, NiO and Pt. The quantification was performed by considering a homogeneous distribution of the species across the sample depth.

Aberration-corrected high-angle annular dark-field scanning transmission electron microscopy (HAADF-STEM) and elemental mapping analysis were performed using a FEI Themis Z microscope equipped with a spherical aberration corrector and operated at 300 kV.

2.3 XRD characterization

X-ray diffraction (XRD) spectra were acquired with a PANalytical X'PERT PRO diffractometer, employing Cu Kα radiation (λ = 1.54187 Å) and a PW3088/60-graded multilayer parabolic X-ray mirror for Cu radiation. The TNTAs were used directly as samples for the acquisition of the diffractograms in the 2θ range from 20 to 95°, at room temperature, using a continuous scan mode. The phase identification was performed using the QualX2 software and the COD database.[36] The Bragg reflexes of the diffractograms were fitted using GSAS2 software[37] fixing the 2θ-value of the Bragg reflexes at the known position.

2.4 XAS characterization

X-ray absorption analyses were performed at the ESRF beamline BM08 LISA,[38] thanks to CERIC funding under experiment A0811110 (https://doi.org/10.15151/ESRF-ES-1437865085). *In situ* and *ex situ* data were collected at the Ni K-edge to study its coordination and local environment. X-ray radiation was monochromatized using a Si 111 double crystal monochromator, and the beam was focused on the sample using Si-coated mirrors that also worked as a higher-order harmonic suppressor. Data were collected in transmission and fluorescence modes depending on the sample concentration. Transmission data were collected using nitrogen-filled ionization chambers, with a voltage of 1 kV; chamber I0 was placed before the sample to collect the incoming radiation, and a second chamber, I1, collected the transmitted radiation; meanwhile, a

 This journal is © The Royal Society of Chemistry 2026

reference (Ni-foil) was placed after the sample and measured in transmission at the same time (using a third ionization chamber). Fluorescence data on the other hand were collected with a 12 element HPGe detector. XAS data were analyzed with the Demeter package.[39]

2.5 XPS characterization

X-ray photoelectron spectroscopy was utilized to analyse the surface composition of the samples. The samples were mounted on a sample holder using double-sided graphite tape and then introduced into the ultra-high vacuum (UHV) chamber of the XPS system. Within the UHV chamber, a non-monochromatic X-ray source (VSW Scientific Instrument Limited, model TA10, Mg Kα radiation, 1486.6 eV) was located, operating at 144 W (12 kV, 12 mA). The system also included a hemispherical analyzer (VSW Scientific Instrument Limited, model HA100) equipped with a 16-channel detector and a dedicated differential pumping system, allowing acquisition at pressures in the main chamber of up to the 10^{-7} mbar range during data acquisition. The pass energy was configured to 44 eV for survey scans and 22 eV for high-resolution scans. Data analysis was performed using CasaXPS software, with inelastic background subtraction using Shirley's method.[40] Peak fitting was carried out using a combination of Gaussian and Lorentzian functions. Spectral calibration was achieved by referencing the lowest component of the C 1s peak, attributed to adventitious carbon, to 284.8 eV.[41] The fitting of the nickel peak was performed using two complex components, comprising six and five individual subcomponents for $Ni(OH)_2$ and NiO, respectively, following the method proposed by Biesinger *et al.*[42] Quantification of the relative $Ni(OH)_2$ and NiO contributions was performed by integrating the fitted component envelopes following Shirley background subtraction and normalization of the total Ni 2p spectral area.

2.6 ICP characterization

ICP metal loading determination was performed by completely digesting the samples first in aqua regia, and then the leaching solution was analyzed using ICP-MS to determine the metal concentration. The metal concentration was then normalized on the surface area of each sample to determine the mass surface loading.

2.7 Electrochemistry

Electrochemical experiments were performed in a classical three-electrode cell with the Pt(x)NiO(y)/TiNT sample used as a working electrode mounted on a titanium holder, a graphite rod as the counter electrode and a saturated $Ag|AgCl|KCl_{sat}$ electrode as the reference. The electrolyte in all experiments was 1 M KOH (Merck) degassed with nitrogen for at least 30 minutes prior to the experiment. All potentials are reported *versus* the reversible hydrogen electrode (RHE). The voltammetric curves were taken between −1.0 and 0.2 V (*vs.* $Ag|AgCl|KCl_{sat}$) at a scan rate of 20 mV s^{-1}; the hydrogen evolution (HER) linear scan voltammetry (LSV) experiments were executed with the same setup but at potentials between −0.9 and −1.5 V and a scan rate of 5 mV s^{-1}; Tafel curves were obtained in the −0.9 and −1.5 V potential range at a scan rate of 1 mV s^{-1} to ensure quasi-steady state conditions.

3. Results and discussion

3.1 Sample description and metal loading

To explore PGM-free HER catalysts, a series of NiO-based samples were prepared by modifying titania nanotubes (TiNTs) using a variable number of nickel oxide ALD deposition cycles. The NiO based samples are designated conventionally as NiO(x)/TiNT samples where the numbers in parentheses indicate the number of ALD cycles. To explore the influence of NiO, we tested samples with a wide nickel oxide concentration range: NiO(15)/TiNT, NiO(80)/TiNT, NiO(180)/TiNT, NiO(360)/TiNT, and NiO(540)/TiNT. For the development of ultralow-Pt HER catalysts, both monometallic and bimetallic samples were included.

The Pt(4)/TiNT sample consists of platinum deposited directly onto TiNT to serve as a reference for Pt-based catalysts. To investigate the effect of combining ultralow amounts of Pt with NiO, two bimetallic samples, Pt(4)NiO80/TiNT and Pt(4)NiO180/TiNT, were prepared by depositing platinum onto supports modified with two different NiO loadings.

A brief summary of the sample series, together with the metal loadings, is presented in Table 1. The uncertainties reported for the EDX-derived metal loadings correspond to the standard deviation of measurements acquired across multiple independent regions of the same sample, reflecting spatial variability of the deposited phases within the porous architecture rather than purely instrumental uncertainty.

The characterization strategy followed a logical sequence aimed at providing a comprehensive understanding of the catalysts' structural, compositional, and electrochemical properties. SEM was initially employed to examine the surface morphology and evaluate the coverage and distribution of the deposited materials.

SEM was followed by an extensive EDX analysis to determine the Pt and NiO concentrations in the samples. TEM

Table 1 Metal loadings of the Pt(y)NiO(x)/TiNT samples

	ALD cycles		EDX-based metal loading (μg cm^{-2})		ICP-based metal loading (μg cm^{-2})	
Sample code	NiO	Pt	Ni	Pt	Ni	Pt
TiNT	—	—	—	—	—	—
NiO(15)/TiNT	15	—	6.2 (1.6)	—	—	—
NiO(80)/TiNT	80	—	11 (2.1)	—	—	—
NiO(180)/TiNT	180	—	25 (2.8)	—	12.1	—
NiO(360)/TiNT	360	—	45 (3.9)	—	—	—
NiO(540)/TiNT	540	—	68 (4.7)	—	—	—
Pt(4)/TiNT	—	4	—	11 (2.1)	—	8.5
Pt(4)NiO(80)/TiNT	80	4	13 (2.0)	8.6 (1.9)	—	—
Pt(4)NiO(180)/TiNT	180	4	26 (3.0)	13 (1.9)	19.3	3.1

investigations were carried out using two complementary techniques: high-resolution TEM (HRTEM) and high-angle annular dark-field scanning transmission electron microscopy (HAADF-STEM).

ICP was used to determine the mass-surface loading in order to normalize the electrochemical data.

HRTEM was used to resolve lattice fringes and gain insights into the crystallinity of the deposited phases, while HAADF-STEM, combined with energy-dispersive X-ray spectroscopy (EDX), provided detailed information about the elemental distribution across the samples.

In Pt-containing catalysts, we also performed probe corrected HAADF-STEM to detect the presence of isolated platinum atoms and assess their dispersion.

XRD measurements were performed to assess the crystallinity of the samples and identify the metal/metal oxide phases. XPS was used to analyze the surface composition and oxidation states of the elements present in the catalysts. For selected samples, XAS at the Ni-edge was conducted to investigate the local atomic environment and coordination of nickel species. Finally, electrochemical characterization (EC) was performed on all samples to evaluate their HER performance.

3.2. Electron microscopy characterization

SEM and HR-TEM provided an initial assessment of the nanotube structure, revealing the distinct morphological features of the deposits. Fig. 2 and 3 present a comparison between the three modified samples: NiO(180)/TiNT (Fig. 2a), Pt(4)NiO (180)/TiNT (Fig. 2b) co-deposited and Pt(4)/TiNT (Fig. 3c).

When a small quantity of Pt was deposited, platinum islands formed on the nanotube surface (Fig. 3c). However, this phenomenon was suppressed when NiO was co-deposited, suggesting a stabilizing effect of NiO on Pt distribution (Fig. S7). In contrast, the deposition of NiO alone resulted in the rounding of nanotube edges, indicative of a substantial accumulation of material on the surface (Fig. S8).

HR-TEM imaging provided localized structural insights, particularly through the analysis of visible lattice fringes *via* fast Fourier transform (FFT). Among the dominant TiO peaks, only a weak NiO (200) reflection, consistent with the Bunsenite reference (RRUFF ID R080121.9), was detected in both the NiO-deposited and NiO/Pt co-deposited samples (Fig. 3g–i)

Unsurprisingly, Pt reflections remained undetectable in the sample where NiO was the sole deposit (Fig. 3e and h). However, in all Pt-only containing samples, we could clearly resolve platinum (111) and (200) fringes directly on the nanoparticles in the HR-TEM images (Fig. 3f and i). This observation confirms the presence of crystalline Pt, despite its apparent suppression when co-deposited with NiO.

STEM-EDX mapping (Fig. 4) provided limited additional structural insights beyond those obtained from HR-TEM for most samples. However, in the Pt(4)/TiNT sample (Fig. 4l), STEM mapping distinctly confirmed the presence of platinum nanoparticles adhering to the nanotube surface.

In the mixed Ni/Pt samples, in contrast, platinum exhibited a homogeneous distribution rather than forming discrete nanoparticle islands (Fig. 4g), strengthening the hypothesis that the co-deposition process facilitated a more uniform dispersion of both elements across the nanotube surface, and hence, that NiO plays a stabilizing role, preventing Pt aggregation and promoting a more evenly distributed platinum phase.

Given the challenges in detecting Pt in the Pt(x)NiO(y) samples, we conducted a more detailed investigation using Cs-corrected STEM microscopy. For comparison, the Pt(4)/TiNT sample was subjected to the same characterization (Fig. 4m). The Cs-STEM analysis confirmed the presence of isolated Pt atoms in both the NiO-containing and Pt(4)/TiNT samples, although less evident, providing direct evidence of atomically dispersed platinum even in the co-deposited samples.

3.3 XRD characterization

X-ray diffraction (XRD) (Fig. S1) analysis was performed on the samples Pt(4)Ni(180)/TiNT, Pt(4)/TiNT, and Ni(360)/TiNT. Measurements were taken from both the front and back of the electrode, with no change between the sides. The diffractograms are presented in Fig. S1; they predominantly exhibit reflections from the underlying metallic titanium, with characteristic peaks at 2θ = 35.1°, 38.2°, and 40.1°, corresponding to

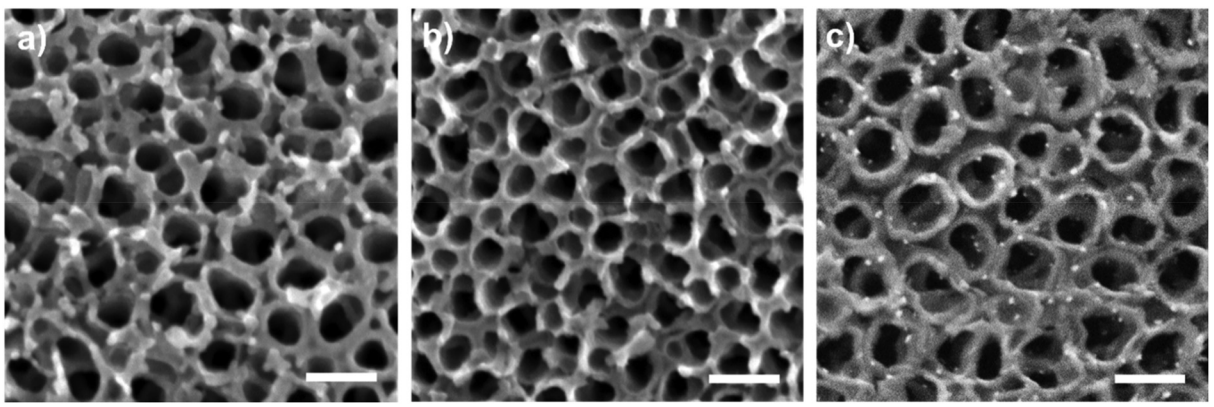


Fig. 2 SEM images of the surfaces of (a) NiO(180)/TiNT; (b) Pt(4)NiO(180)/TiNT; and (c) Pt(4)/TiNT. Scale bar is 100 nm.

 This journal is © The Royal Society of Chemistry 2026

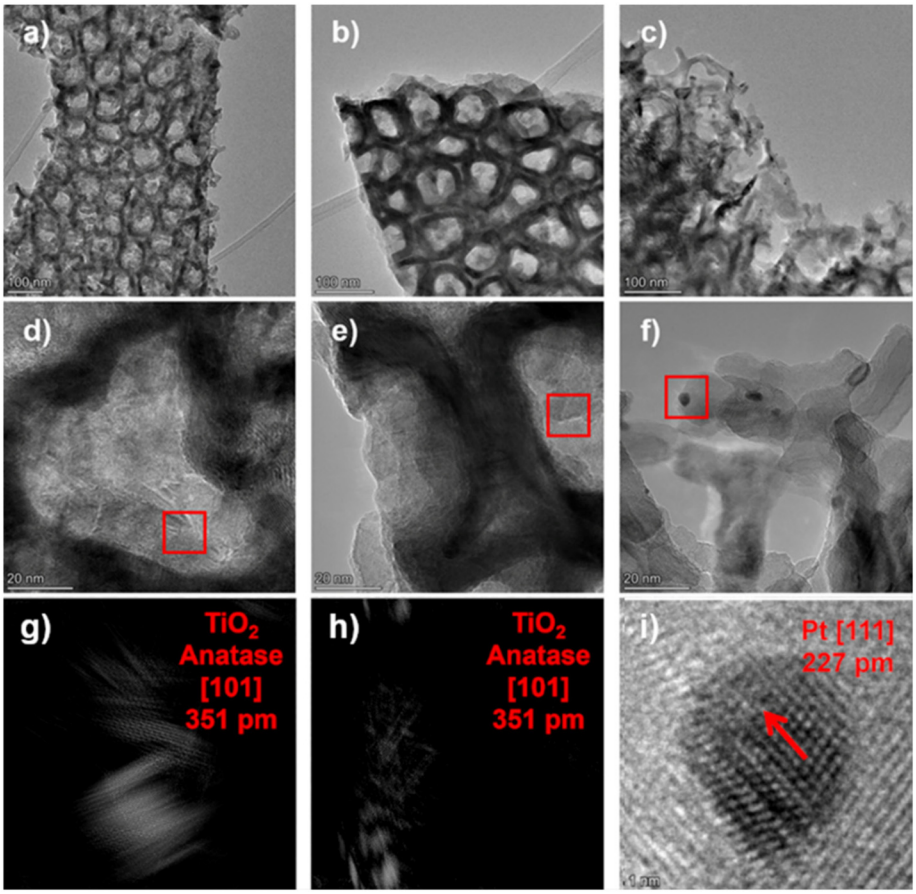


Fig. 3 HRTEM images of the surfaces at different magnifications: (a, d and g) NiO(180)/TiNT; (b, e and h) Pt(4)NiO(180)/TiNT; and (c, f and i) Pt(4)/TiNT.

the (010), (002), and (011) planes, respectively. Additional titanium reflections were observed at 52.9° (012), 62.9° (110), 70.6° (013), 74.1° (020), 76.2° (112), and 77.3° (021).

Beyond titanium, only a weak signal attributed to anatase was detected at 25.3°, consistent with the presence of a thin oxide layer. The limited intensity of the anatase reflections can be explained by two key factors: (i) the oxide layer's minimal thickness (<200 nm), which is approximately two orders of magnitude smaller than the titanium fibers, and (ii) the shallow penetration depth of X-rays in titanium-based materials. At the Cu Kα emission line, the attenuation length of X-rays in titanium is approximately 10 μm at normal incidence and only 3.7 μm at a 20° angle, indicating that XRD primarily probes the topmost surface of the electrode. Notably, no detectable reflections corresponding to Ni or Pt species were observed in any of the samples, despite their confirmed presence through other characterization techniques. The absence of NiO reflections can be attributed to two primary factors: (i) its amorphous nature and (ii) its low loading, combined with (iii) the inherent X-ray attenuation in titanium-based materials.

For Pt, the lack of observable reflections is primarily due to its low loading and high dispersion, a behaviour consistent with previous studies on similarly low-loaded noble metals. In analogous systems, XRD failed to detect ruthenium due to its low concentration, while palladium at a loading of 1.7 mg cm^{-2} was barely visible, and at 80 μg cm^{-2}, it remained entirely undetectable.[41] Given that the Pt content in the present study is even lower, its absence in the XRD patterns is expected.

3.4. XAS characterization

Understanding the local structure of oxidized Ni is crucial in order to understand the effect on Pt, particularly given its undetectability by XRD. The absence of NiO reflections suggests either an amorphous nature or an extremely small crystallite size, preventing the identification of a long-range order. However, this does not preclude the presence of well-defined local coordination environments. To overcome these limitations, X-ray absorption spectroscopy (XAS) was employed at the Ni K edge (8333 eV) to probe the short-range order of Ni species, providing insights into their electronic structure, oxidation state, and coordination geometry. By comparing *ex situ* and *in situ* XANES data of fresh and spent samples with reference materials, and by fitting the EXAFS spectra, we were able to assess the degree of disorder in the Ni environment and determine whether structural changes occurred under the reaction conditions.

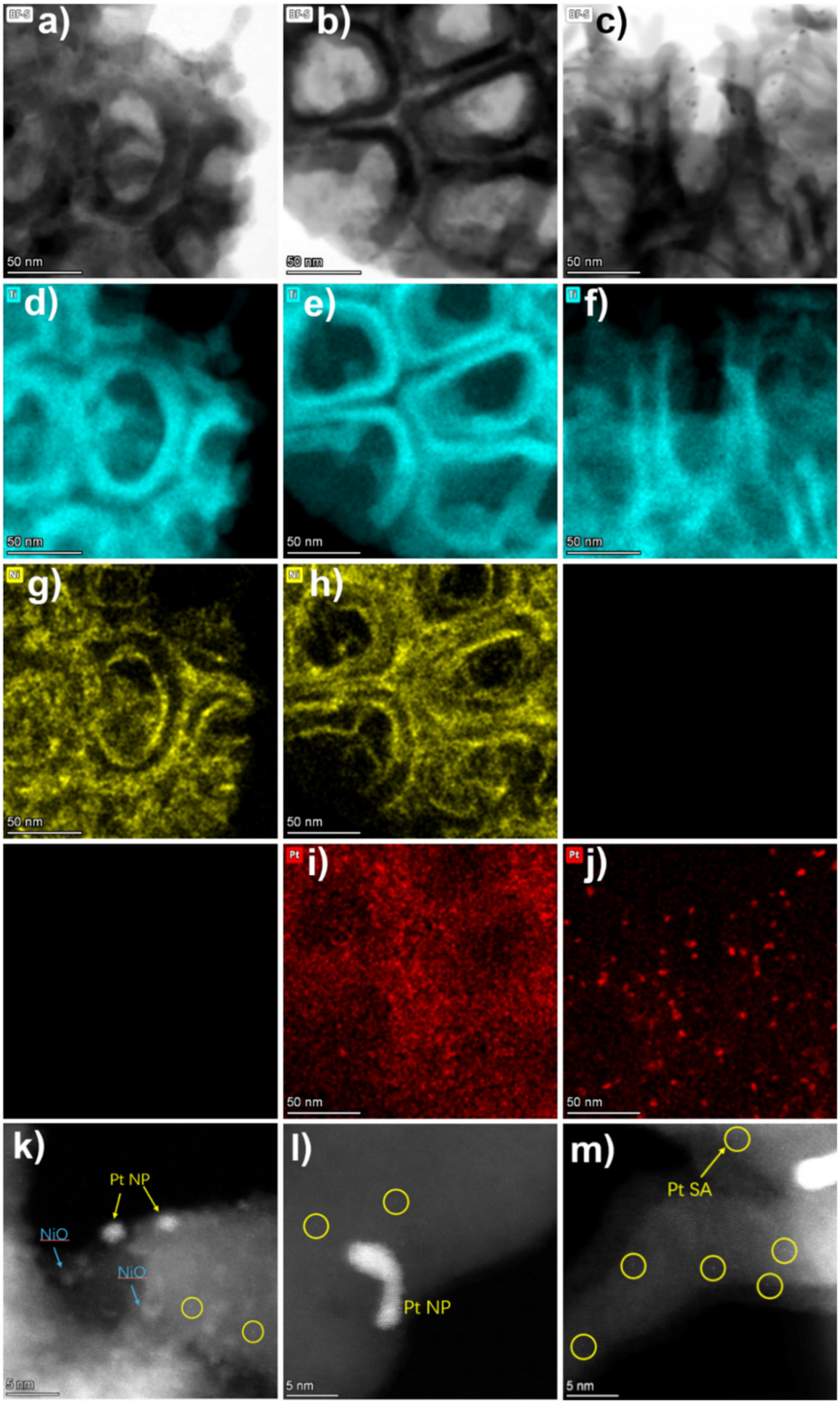


Fig. 4 STEM-EDX mapping of Ni(360)/TiNT (a, d and g), Pt(4)Ni180/TiNT (b, e, h and i) and Pt(4)/TiNT (c, f, j and m) samples; Cs corrected STEM images of Pt(4)/TiNT (l and m) and Pt(4)Ni(180)/TiNT (k).

The *ex situ* study has mostly shown correspondence with the $Ni(OH)_2$ phase, as can be observed from the XANES and EXAFS data, Fig. 5a and b, which compare the NiO(540)/TiNT sample with the reference phase. However, a comparison with the EXAFS Fourier transform (Fig. 5c) spectra shows some differences with the $Ni(OH)_2$ reference. We can in fact notice a

 This journal is © The Royal Society of Chemistry 2026

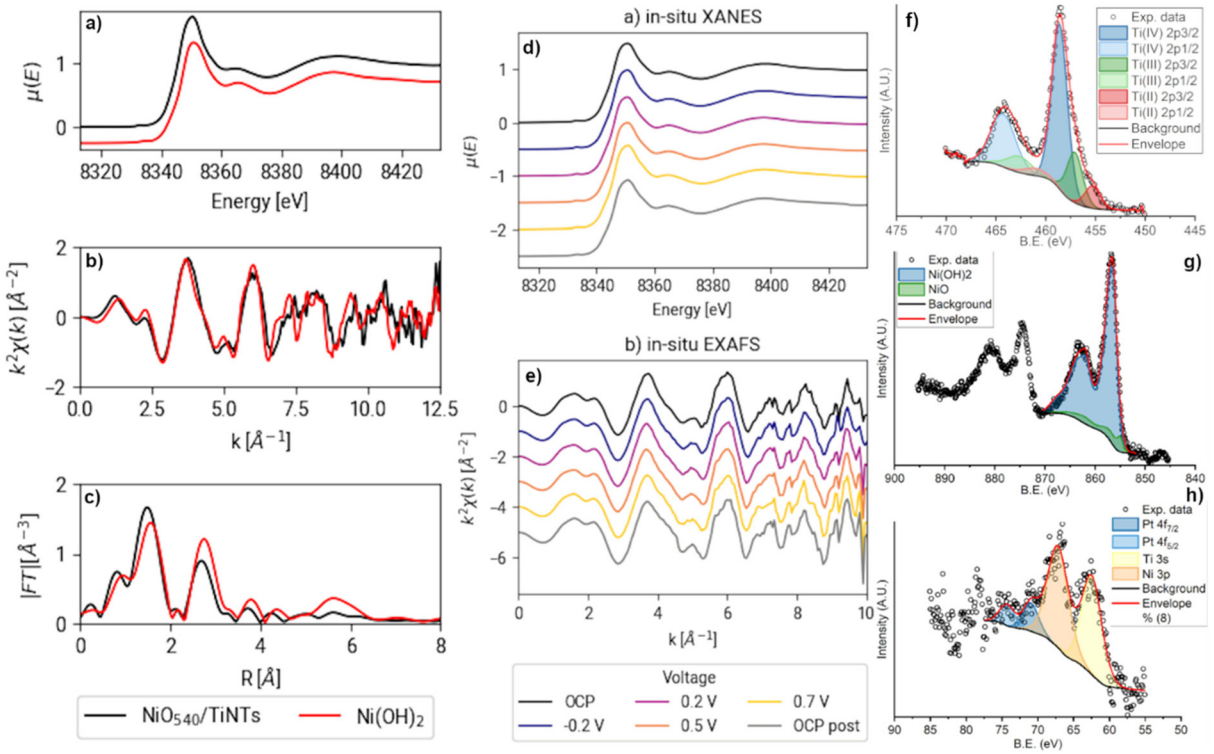


Fig. 5 (a, b and c) XAS of NiO(540)/TiNTs compared to the $Ni(OH)_2$ reference sample; (d and e) *in situ* XANES and EXAFS characterization; and (f, g and h) XPS characterization of Pt(4)NiO(180)/TiNT for Ti, Ni and Pt edges.

small shift in the signal of Ni–O (2.06 Å) and Ni–Ni (2.95 Å) and that no signal at 5.5 Å (second Ni–Ni shell) can be observed, suggesting a lowering of the structure's order at large distances. The fit of the EXAFS signal (Table S1) has confirmed the correspondence with the $Ni(OH)_2$ structure. Even though the fit Ni–O interatomic distance is not resolutive (the theoretical values are 2.06 Å for $Ni(OH)_2$ and 2.09 Å for NiO), the Ni–Ni distance, 3.07 Å, is clearly longer than the one tabulated for NiO (2.95 Å) and much closer to that of $Ni(OH)_2$, 3.13 Å. *In operando* analysis (Fig. 5d and e) shows no significant changes in Ni coordination or local environments with the potential. Different XAS Ni K edge acquisitions were performed targeting the sample immersed in 1 M NaOH in a three electrode electrochemical cell, and applying increasing potential steps (sequentially OCP, −0.2 V, 0.2 V, 0.5 V, and 0.7 V *vs.* RHE, and again OCP) in order to force Ni oxide/hydroxide formation. The fitting of the EXAFS FT, Fig. S2, and Table S1 showed no change of Ni–O interatomic distances; however, we observed an increase of the Ni–Ni distance to 3.11(2) within the adopted potential range, compatible with the interatomic distances of $Ni(OH)_2$. The absence of a change may be due to (I) no change occurring in the structure during the potential scan, or (II) changes affecting only the material's surface, or a small portion of the material, and not observable *via* XAS analysis, which probes both the bulk and the surface. The first is more likely, as a change in the oxidation number of nickel expected with the formation of Ni^{3+} requires higher potentials than 0.8 V RHE attained during the *in situ* EXAFS analysis.[43] The *in operando* XAS results therefore support the interpretation that Ni species remain predominantly in a $Ni(OH)_2$-like coordination environment throughout the HER-relevant potential range, consistent with a role as a structurally stable interfacial promoter and proton-transfer mediator rather than as a bulk redox-active phase.

3.5 XPS characterization

The catalytic properties of anatase-based materials are highly dependent on their purity, particularly the oxidation state of titanium and the presence of oxygen vacancies. To investigate these aspects, X-ray photoelectron spectroscopy (XPS) was employed to analyse the TNTA-web nanotubes alone (Fig. 6f). The Ti 2p transition revealed binding energies of 458.8 eV for Ti $2p_{3/2}$ and 464.4 eV for Ti $2p_{1/2}$, values characteristic of Ti^{4+} in TiO_2. In this reference sample, no signals corresponding to lower oxidation states, such as Ti^{3+} (457.6 eV) or Ti^{2+} (455.4 eV), were detected, confirming the absence of significant oxygen vacancies or reduced titanium species. On the other hand, in the spectra of the NiO(540)/TiNTs sample, small signals at low energies, attributable to Ti^{3+} and Ti^{2+}, were detected. Nevertheless, Ti^{4+} remains the principal component, accounting for approximately 70% of the total area, while Ti^{3+} and Ti^{2+} represented about 20% and 10%, respectively.[44]

Beyond titanium, XPS characterization provided insight into the chemical nature of the electrocatalyst components.

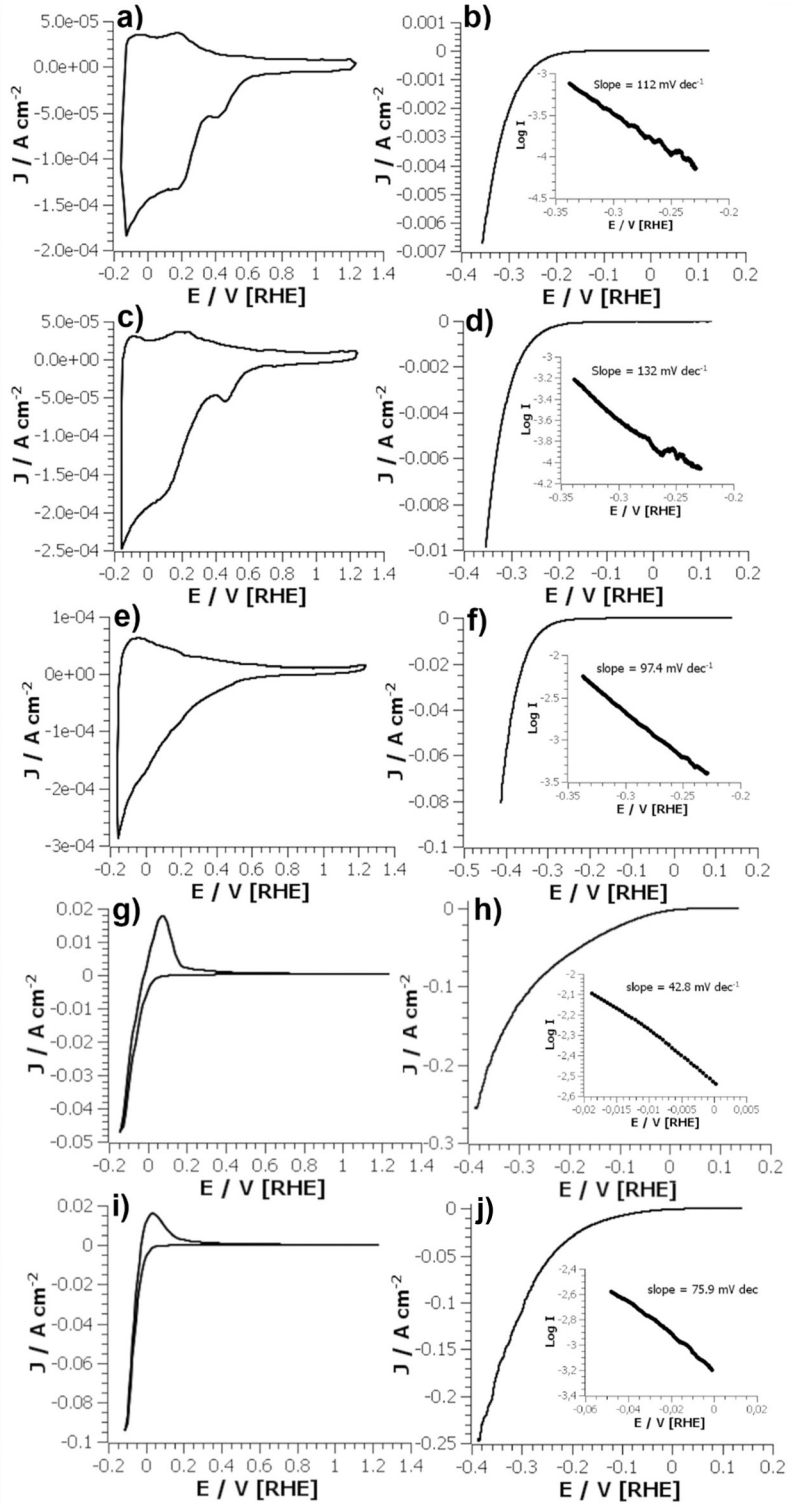


Fig. 6 Cyclic voltammetry, LSV and Tafel curves of the ALD materials. (a and b) Ni(80); (c and d) NiO(180); (e and f) Ni(360); (g and h) Pt(4)/TiNT; and (i and j) Pt(4)NiO(180)/TiNT.

The deconvolution of the Ni 2p spectrum (Fig. 5g) confirmed that nickel is predominantly present as $Ni(OH)_2$ on the surface, with a minor fraction in the form of NiO. This distinction is particularly relevant, as the presence of $Ni(OH)_2$ near platinum could facilitate the hydrogen evolution reaction by providing local proton sources. Regarding Pt, however, XPS analysis did not clearly detect the presence of platinum in the Pt(4)/TiNT and Pt(4)NiO(180)/TiNT samples, as the Pt $4f_{5/2}$ and

 This journal is © The Royal Society of Chemistry 2026

$4f_{7/2}$ transitions did not display sufficient intensity to be clearly distinguished from the background noise (around 1σ), although their signal may suggest its presence. This can be ascribed to the very low loading of platinum in those materials. Notably, comparative analysis of the NiO(360)/TiNT and Pt(4)NiO(180)/TiNT samples (Fig. S3 and S4) revealed that the chemical state of nickel was not significantly altered by the presence of the other metal species in either sample, indicating their stability in the final material.

Surface-sensitive XPS quantification (Table S2), together with ICP-MS mass loading analysis (Table 1), provides the most representative compositional description for these catalysts, considering the ultrathin ALD overlayers deposited onto TiO_2 nanotube arrays. XPS analysis confirms that Pt is intentionally present as a minor surface component across all samples, whereas Ni-containing materials exhibit substantial surface enrichment in Ni species, consistent with the designed role of NiO as a surface modifier and co-catalyst for ultralow Pt deposition. ICP-MS quantification further shows that the Pt loading in Pt(4)NiO(180)/TiNT is approximately one-third of that measured for the monometallic Pt(4)/TiNT reference. Importantly, the introduction of NiO does not merely dilute Pt content but strongly influences Pt dispersion. In the absence of NiO, Pt forms discrete islands on the nanotube surface, whereas co-deposition with NiO suppresses island formation, with Cs-corrected STEM confirming the presence of highly dispersed, including isolated, Pt species. This structural transformation is consistent with a stabilising effect induced by the surface-dominant $Ni(OH)_2$ phase identified by Ni 2p XPS deconvolution. A possible explanation of this phenomenon can be the better interaction between the Pt and the $Ni(OH)_2$ phases, which reduces Pt mobility and risk of aggregation, while also improving catalyst stability. Furthermore, the interaction of the precursor with the nickel phase can be another reason for better Pt dispersion due to the possible increase in the nucleation sites. The improved Pt dispersion directly correlates with the electrochemical behaviour: despite containing only approximately one-third of the Pt loading, Pt(4)NiO(180)/TiNT surpasses Pt(4)/TiNT at higher cathodic overpotentials, demonstrating significantly enhanced Pt utilisation efficiency and better stability.

XPS analysis did not clearly detect the presence of platinum in the Pt(4)/TiNT and Pt(4)NiO(180)/TiNT samples, as the Pt $4f_{5/2}$ and $4f_{7/2}$ transitions did not have sufficient intensity to be clearly distinguished from the background noise (around 1σ), although weak features hint at its presence. This is consistent with the ultralow Pt loadings (~8.5 μg cm^{-2} for Pt(4)/TiNT and ~3.1 μg cm^{-2} for Pt(4)NiO(180)/TiNT, confirmed by ICP), which correspond to surface concentrations well below 0.1 at%. The three-dimensional porous architecture of the TiNT/Ti-web electrode further distributes Pt over a large internal surface area, compounding the sensitivity challenge inherent to the low total loading. Determination of the Pt oxidation state and local coordination environment by complementary synchrotron methods also proved unfeasible in this material system. Specifically, Pt L_3-edge X-ray absorption spectroscopy (XANES/EXAFS) was attempted but could not yield usable data for the following reasons: (i) the metallic titanium support is X-ray opaque at the Pt L_3-edge energy (~11.564 keV), rendering transmission-mode acquisition impossible; (ii) the porous three-dimensional Ti matrix generates intense elastic and Compton scattering that overwhelms the weak Pt Lα fluorescence signal (~9.44 keV) in fluorescence mode at these ultralow loadings; and (iii) again the Pt content confirmed by ICP is below the practical sensitivity threshold for fluorescence-mode Pt L-edge XAS on a high-*Z*, scattering the matrix support. Consequently, no assignment of the Pt oxidation state or coordination environment is made in this work.

3.6. Electrochemistry

Fig. 6a, c, e, g, i and Fig. S5 show the cyclic voltammetry curves in 1 M KOH electrolyte in the −0.2–1.2 V *vs.* RHE range; the hydrogen adsorption peak can be clearly distinguished in the Pt(4)/TiNTs, Pt(4)NiO(80)/TiNTs and Pt(4)NiO(180)/TiNTs samples; in addition, the onset potential of the HER is shifted to less cathodic potentials when platinum is present. The NiO (*x*)/TiNTs samples with increasing loading first show (x = 15) a cathodic peak at 0.2 V *vs.* RHE that decreases in x = 80 shifting to cathodic potential in x = 180 and then disappearing in the x = 360 and 540 samples. Another NiO reduction peak is centered at 0.35 V in the NiO(15)/TiNT sample, shifting progressively to anodic potentials (it is centered 0.45 V in the x = 180 sample) disappearing at higher TiNT coverage (x = 360 and 540).

The LSV polarization data for the HER (Fig. 6b, d, f, h, l; Table 2 and Table S6) of the NiO(x)/TiNT series show a clear trend of increasing current density as the Ni loading increases from x = 15 to x = 360, whereas the sample with x = 540 does not exhibit any further appreciable improvement. This indicates that the HER activity benefits from increasing NiO loading up to an optimal coverage, beyond which additional NiO mainly leads to overcoverage and does not translate into enhanced performance. The onset potentials (*vs.* RHE), calculated using 1 mA cm^{-2} as the threshold current, are −369 mV, −286 mV, −283 mV, −255 mV and −253 mV for NiO(x)/TiNTs with x = 15, 80, 180, 360 and 540, respectively. The lowest potential required to reach 50 mA cm^{-2} for the NiO(x)/TiNT series is −377 mV *vs.* RHE, compared with the much lower overpotential of −168 mV *vs.* RHE attained by the Pt(4)/TiNT sample at the same current density. Mass-specific normalized currents at −50 mV, −150 mV and −300 mV clearly show the effect of the presence of NiO on the HER performance of the material, with Pt(4)NiO(180)/TiNT outperforming Pt(4)/TiNT at higher cathodic overpotentials. Differential capacitance measurements (Fig. S9) do not show a marked increase in the surface area with the addition of Pt to the nickel oxide matrix, as the differential capacitance of Pt(4)NiO(180)/TiNT is even smaller compared to that of the NiO(180)/TiNT material. In addition, comparing the differential capacitances of Pt(4)NiO (180)/TiNT and Pt(4)/TiNT, the differential capacitance of the latter seems to indicate that the surface area of Pt(4)NiO(180)/TiNT is smaller than the Pt-only material, suggesting that the

Table 2 Relevant electrochemical LSV data for atomic layer deposited TiNT materials

				Mass-specific currents A g_{Pt}^{-1}		
	E_{onset} (1 mA cm^{-2})	E@10 mA cm^{-2}	E@50 mA cm^{-2}	E = −50 mV	E = −150 mV	E = −300 mV
NiO(15)/TiNT	−369 mV	—	—	—	—	—
NiO(80)/TiNT	−286 mV	−405 mV	—	—	—	—
NiO(180)/TiNT	−283 mV	−399 mV	—	—	—	—
NiO(360)/TiNT	−255 mV	−330 mV	−377 mV	—	—	—
NiO(540)/TiNT	−253 mV	−336 mV	−402 mV	—	—	—
Pt(4)/TiNT	−17.0 mV	−51.1 mV	−168 mV	1.15	4.53	14.4
Pt(4)NiO(80)/TiNT	−37.0 mV	−133 mV	−276 mV	—	—	—
Pt(4)NiO(180)/TiNT	−13.0 mV	−43.8 mV	−132 mV	0.95	5.00	35.7

increase in performance is not due to an increase in the electrochemical surface area.[45,46] Tafel slopes for NiO(80)/TiNT, NiO(180)/TiNT and NiO(360)/TiNT are very similar, consistent with a Volmer–Heyrovsky mechanism with the Volmer step (first hydride formation) being rate determining for the Ni-based materials.[47]

The NiO(x)/TiNT series has already demonstrated that the HER activity progressively increases with Ni loading up to an optimal surface coverage, beyond which additional NiO does not provide further significant improvements, indicating an intrinsic catalytic contribution of the NiO phase. In the bimetallic series, increasing NiO co-deposition systematically improves the HER response, and the Pt–NiO catalysts consistently outperform both monometallic references over the investigated potential range, confirming a synergistic rather than purely additive effect. In particular, Pt utilisation efficiency is substantially enhanced, approaching a threefold improvement relative to Pt(4)/TiNT. A distinct latency effect is observed at low overpotentials, where the current density of Pt(4)NiO(x)/TiNT initially increases more slowly than that of Pt(4)/TiNT. This behaviour is consistent with partial attenuation of the Schottky junction at the Pt–TiO_2 interface induced by the presence of NiO. At higher cathodic overpotentials, however, the beneficial contribution of NiO_x becomes dominant, and Pt(4)NiO(180)/TiNT ultimately surpasses the monometallic Pt reference. The interfacial synergy between NiO, Pt, and TiO_2 is supported by three complementary observations. First, surface Ni$(OH)_2$ species provide local proton sources that facilitate the rate-determining Volmer step, consistent with both the Tafel analysis and the *in operando* XAS results, which show no significant changes in Ni coordination within the investigated potential range. Second, NiO appears to electronically modify the Pt–TiO_2 interface through modulation of the Schottky junction behaviour, although direct probing of interfacial charge transfer and electronic structure would require complementary approaches such as valence-band spectroscopy or theoretical calculations. Third, the NiO matrix suppresses Pt aggregation and mitigates Pt leaching, resulting in a degradation rate approximately eight times lower than that measured for Pt(4)/TiNT during prolonged galvanostatic operation. In sharp contrast, the Pt(4)NiO(i)/TiNT samples display markedly superior HER performances. The onset potentials (at 1 mA cm^{-2}) for Pt(4)NiO(80)/TiNT and Pt(4)NiO(180)/TiNT are −37 mV and −13 mV *vs.* RHE, respectively, compared to 20 mV *vs.* RHE for Pt(4)/TiNT. Although Pt(4)/TiNT displays a slightly more positive onset potential, the Pt(4)NiO(180)/TiNT sample rapidly surpasses Pt(4)/TiNT in current density as the potential becomes more cathodic (Table 2), despite containing significantly less Pt (one deposition cycle instead of four). This behavior is consistent with the more uniform and finely dispersed distribution of Pt on the NiO-modified TiNTs, as revealed by the morphological and structural characterization, which likely maximizes the effective utilization of Pt active sites.

A broader comparison with recently reported low-Pt and transition-metal-based alkaline HER catalysts is provided in Table S3. Despite the extremely low Pt loading employed in the present study, the Pt(4)NiO(180)/TiNT catalyst achieves competitive HER activity together with substantially improved operational stability at high current density. In particular, the combination of hierarchical transport architecture, highly dispersed Pt species, and $Ni(OH)_2$-rich interfaces enables performance levels comparable to those of significantly higher noble-metal-loaded systems while maintaining enhanced long-term stability.

It is worth noting that the Pt–NiO-based materials show a certain "latency" in current increase at less cathodic potentials when compared to Pt(4)/TiNT, despite the broadly comparable onset region. This behaviour could possibly be attributed to Schottky junction effects at the metal–semiconductor interface. It is reasonable to consider that Pt(4)/TiNT can exhibit a pronounced Schottky junction due to the significant difference in the work function between Pt and TiNT TiO_2 interfaces (Φ_{Pt} ≈ 6 eV *vs.* Φ_{TiO2} ≈ 4.0 eV).[48–50] In contrast, the initial Schottky-driven enhancement near the onset potential could be less pronounced for Pt(4)NiO(x)/TiNT due to the presence of NiO, leading to the observed "latency" in the low-overpotential region when compared to Pt(4)/TiNT. At more cathodic potentials, however, the beneficial electrocatalytic contribution of NiO_x, which provides additional active sites and possible synergistic interactions with Pt, dominates, and the Pt(4)NiO(180)/TiNT sample ultimately outperforms Pt(4)/TiNT in HER activity.[50] Tafel analysis (Fig. 6f, h and l) further supports this behaviour. The NiO(360)/TiNT sample exhibits a Tafel slope of 97 mV dec^{-1}, while the Pt-containing Pt(4)NiO(180)/TiNT shows a Tafel slope of 72.9 mV dec^{-1}. Both values are consist-

 This journal is © The Royal Society of Chemistry 2026

ent with a Volmer–Heyrovsky mechanism with the Volmer step (proton discharge and first hydride formation) being rate determining.[20,22,47,51,52] In contrast, Pt(4)/TiNT displays a significantly lower Tafel slope of 42.8 mV dec^{-1}, indicative of a Volmer–Heyrovsky mechanism in which the Heyrovsky step (electrochemical desorption) is rate determining for the HER. This shift in the rate-determining step upon introducing NiO_x and reducing Pt loading highlights the distinct interfacial kinetics and the crucial role of the composite metal/oxide/semiconductor architecture in governing HER performance. While the exact Pt oxidation state and coordination environment remain undetermined due to the analytical constraints described in section 3.4, the electrochemical behaviour is consistent with highly dispersed, catalytically active Pt species serving as H_2 desorption sites. Under the cathodic potentials applied during the HER, *in situ* reduction of any initially oxidized Pt species to metallic Pt^0 is plausible, which would provide the necessary electronic structure for efficient H–H bond formation and H_2 release.

The NiO(x)/TiNT series has already shown that the HER activity improves progressively with nickel loading up to an optimal coverage, beyond which overcoverage limits further gains, establishing an intrinsic contribution of NiO to catalytic activity. In the bimetallic series, increasing NiO co-deposition content systematically improves the onset potential, and the bimetallic catalysts consistently outperform both monometallic references across the full potential range, confirming synergistic rather than additive enhancement, with platinum utilisation improved by a factor approaching three. A latency effect at low overpotentials, where current density increases more slowly than for Pt(4)/TiNT, reflects attenuation of the Schottky junction at the Pt–TiO_2 interface by NiO; at higher overpotentials, the contribution of NiO_x dominates and Pt(4)NiO(180)/TiNT ultimately prevails. The interfacial synergy is supported by three independent lines of evidence discussed in the paper: chemically, surface $Ni(OH)_2$ provides local proton sources facilitating the rate-determining Volmer step, as supported by Tafel analysis and confirmed by *in operando* XAS, which shows no change in nickel coordination across the relevant potential window; electronically, NiO modulates the Schottky junction as described above; and structurally, the NiO matrix prevents Pt aggregation and leaching, yielding a degradation rate approximately eight times lower than that of Pt(4)/TiNT over more than fifty hours of continuous operation.

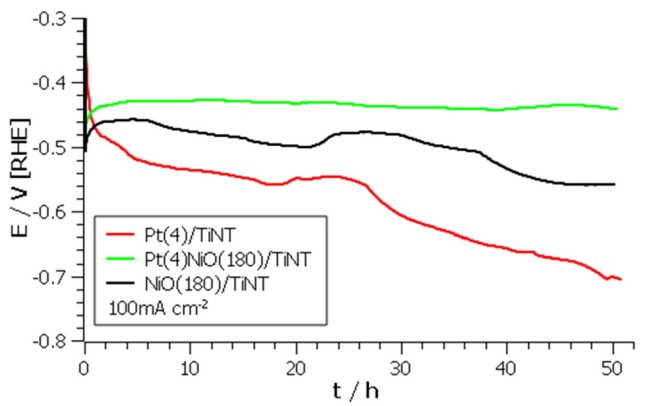


Fig. 7 Chronopotentiometry experiments performed at 100 mA cm^{-2} current density.

Regarding the stability of the materials under continuous operation, Pt(4)NiO(180)/TiNT greatly outperforms Pt(4)/TiNT. The average potential slope at 100 mA cm^{-2} is −4.6, −0.8 and −0.6 mV h^{-1}, respectively, for Pt(4)/TiNT, NiO(180)/TiNT and Pt(4)NiO(180)/TiNT indicating that the NiO matrix prevents platinum leaching or aggregation (Fig. 7).

4. Conclusions

In this study, we successfully engineered hydrogen evolution reaction (HER) electrocatalysts by utilizing atomic layer deposition (ALD) to deposit nickel oxide (NiO) and platinum nanoparticles onto titania nanotube (TiNT) arrays, embedded within a porous titanium sintered web. This innovative approach produced dual-scale porosity, significantly enhancing catalyst dispersion and active site accessibility. Such structural advantages provide pathways toward both platinum-group metal (PGM)-free and ultra-low PGM catalysts, crucial for reducing costs and reliance on scarce resources in green hydrogen production.

Comprehensive characterization using high-resolution transmission electron microscopy (HR-TEM), high-angle annular dark-field scanning transmission electron microscopy (HAADF-STEM), X-ray photoelectron spectroscopy (XPS), and X-ray absorption spectroscopy (XAS) confirmed that nickel predominantly exists as $Ni(OH)_2$. This chemical state was essential in optimizing catalytic interactions. A wide range of catalysts were developed and assessed, spanning from completely PGM-free NiO-only systems to ultra-low platinum loadings, specifically approximately 8.6 μg cm^{-2} in Pt(4)NiO(80)/TiNT and 13 μg cm^{-2} in Pt(4)NiO(180)/TiNT.

Notably, these co-deposited Pt-NiO catalysts demonstrated better HER performance relative to their monometallic platinum counterparts, suggesting a strong synergistic effect where $Ni(OH)_2$ stabilizes and enhances the dispersion of Pt nanoparticles, effectively reducing their aggregation. This improved dispersion directly correlates with enhanced catalytic efficiency.

Electrochemical studies further identified that optimal NiO loading was approximately 45 μg cm^{-2} (NiO(360)/TiNT), delivering a competitive HER overpotential of −377 mV at a current density of 50 mA cm^{-2}. Beyond this loading, further increases resulted in negligible benefits, highlighting the necessity of precisely tuning the catalyst loading to maximize activity.

Crucially, the Pt(4)NiO(180)/TiNT catalyst achieved remarkable HER performance with an overpotential of just −132 mV at 50 mA cm^{-2}. This value closely rivals that of the monometallic Pt(4)/TiNT catalyst (−168 mV at the same current density), despite significantly lower platinum usage. Mechanistically, Tafel analysis indicated a Volmer–Heyrovsky reaction mecha-

nism across the samples, with $Ni(OH)_2$ notably accelerating the Heyrovsky desorption step, crucial for enhanced HER kinetics on platinum surfaces.

Beyond the specific HER metrics, this work introduces an intrinsically versatile materials platform in which ALD-enabled control over phase composition, dispersion, and interfacial architecture is integrated within a mechanically robust, industrially relevant titanium porous transport layer. The embedded TiNT framework, combined with tunable NiO and Pt loadings, offers a general strategy for designing next-generation electrodes where catalytic phases, support morphology, and transport properties are co-optimized rather than treated as separate problems. Such an approach is directly translatable to a broader class of alkaline and AEM-based devices, and can be extended to other catalytic chemistries (*e.g.* oxygen electrocatalysis or small-molecule oxidation) by simply replacing or combining the active phases. In this sense, the present system acts as a model blueprint for dispersion-controlled, PGM free and ultralow-PGM architectures that combine high performance with critical resource saving to provide a significant opportunity for scalability.

Author contributions

Jonathan Filippi: conceptualization, formal analysis, visualization, investigation, writing – original draft, and writing – review & editing; Nicola Calisi: investigation and formal analysis; Laura Capozzoli: investigation; Stefano Caporali: investigation and formal analysis; Francesco D'Acapito: investigation and formal analysis; Jacopo Orsilli: investigation and formal analysis; Ilaria Perissi: writing – review & editing; Carlo Santoro: validation and investigation; Mohsin Muhyuddin: investigation; Francesco Vizza: supervision, validation, and funding acquisition; Yong Qin: investigation; Jiankang Zhang: investigation, formal analysis, and writing – review & editing; Alessandro Lavacchi: conceptualization, supervision, validation, visualization, funding acquisition, and writing – review & editing; Enrico Berretti: conceptualization, investigation, formal analysis, visualization, and writing – review & editing.

Conflicts of interest

The authors declare no conflicts of interest.

Data availability

Raw data were generated at the CNR-ICCOM (Florence, Italy), CNR-IOM Sec. Grenoble c/o ESRF-The European Synchrotron (France) and the National Interuniversity Consortium of Materials Science and Technology (Florence, INSTM). Data generated consist of electrochemical tests, spectroscopic characterization (XAS, *etc.*) and microscopic characterization. Raw and derived data produced during this study are available from the corresponding author (Alessandro Lavacchi, alessandro.lavacchi@iccom.cnr.it) on request.

Supplementary information contain additional XRD, EXAFS, SEM, HRTEM and Electrochemical data; also a comparison of performances with similar methods reported in literature are included. Supplementary information (SI) is available. See DOI: https://doi.org/10.1039/d5nr05314e.

Acknowledgements

This research was funded by the MIUR with PRIN 2022 "From metal nanoparticles to molecular complexes in electrocatalysis for green hydrogen evolution and simultaneous fine chemicals production (FUTURO)" Prot. 2022NW4P2T, European Union Next-Generation EU (PIANO NAZIONALE DI RIPRESA E RESILIENZA (PNRR)), Missione 2, Investimento 3.5, and Progetto "PERMANENT-Materiali e componenti avanzati per celle a combustibile PEM con innovativa strutturazione multiscala per il miglioramento di durabilità e stabilità" Decreto del Ministro della Transizione Ecologica del 23.12.2021, articolo 1, comma 5, lettera A. Prog. n. RSH2A_000012 – CUP: F47G22000290006. C. S. and M. M. would like to also acknowledge the European Union, NextGeneration EU from the Italian Ministry of Environment and Energy Security POR H2 AdP MMES/ENEA with involvement of CNR and RSE, PNRR – Mission 2, Component 2, Investment 3.5 "Ricerca e sviluppo sull'idrogeno", CUP: I93C22001170006 under the ENEA – UNIMIB agreement (Procedure 1.1.3 PNRR POR H2), project "Study and development of electrocatalysts of the type Pt-TM/C (TM = Co, Fe, Ni) in the cathode of a PEM-WE.". The authors also acknowledge the CERIC-ERIC Consortium for financial support for the access to the European Synchrotron Radiation Facility (ESRF), for provision of synchrotron radiation facilities under proposal A08-1-1110 on beamline BM-08.

References

1 M. Filonchyk, M. P. Peterson, L. Zhang, V. Hurynovich and Y. He, *Sci. Total Environ.*, 2024, **935**, 173359.
2 World Energy Transitions Outlook 2024.
3 N. Mlilo, J. Brown and T. Ahfock, *Technol. Econ. Smart Grids Sustainable Energy*, 2021, **6**, 25.
4 J. Rugolo and M. J. Aziz, *Energy Environ. Sci.*, 2012, **5**, 7151.
5 M. Chatenet, B. G. Pollet, D. R. Dekel, F. Dionigi, J. Deseure, P. Millet, R. D. Braatz, M. Z. Bazant, M. Eikerling, I. Staffell, P. Balcombe, Y. Shao-Horn and H. Schäfer, *Chem. Soc. Rev.*, 2022, **51**, 4583–4762.
6 R. R. Wang, Y. Q. Zhao, A. Babich, D. Senk and X. Y. Fan, *J. Cleaner Prod.*, 2021, **329**, 129797.
7 D. Saygin, H. Blanco, F. Boshell, J. Cordonnier, K. Rouwenhorst, P. Lathwal and D. Gielen, *Sustainability*, 2023, **15**, 1623.
8 S. Schlehuber, M. Gutsch, N. Kronemeyer, F. Frieden and S. Von Delft, *Commun. Eng.*, 2025, **4**, 50.
9 Hydrogen technology predictions for 2025.
10 I. Perissi and A. Jones, *Sustainability*, 2022, **14**, 4728.

 This journal is © The Royal Society of Chemistry 2026

11 N. Dubouis, D. Aymé-Perrot, D. Degoulange, A. Grimaud and H. Girault, *Joule*, 2024, **8**, 883–898.
12 C. Santoro, A. Lavacchi, P. Mustarelli, V. Di Noto, L. Elbaz, D. R. Dekel and F. Jaouen, *ChemSusChem*, 2022, **15**, e202200027.
13 T. Wang, X. Cao and L. Jiao, *Carbon Neutrality*, 2022, **1**, 21.
14 C. R. Wang, J. M. Stansberry, R. Mukundan, H.-M. J. Chang, D. Kulkarni, A. M. Park, A. B. Plymill, N. M. Firas, C. P. Liu, J. T. Lang, J. K. Lee, N. E. Tolouei, Y. Morimoto, C. Wang, G. Zhu, J. Brouwer, P. Atanassov, C. B. Capuano, C. Mittelsteadt, X. Peng and I. V. Zenyuk, *Chem. Rev.*, 2025, **125**, 1257–1302.
15 E. Schropp, F. Campos-Carriedo, D. Iribarren, G. Naumann, C. Bernäcker, M. Gaderer and J. Dufour, *Appl. Energy*, 2024, **356**, 122247.
16 D. Hua, J. Huang, E. Fabbri, M. Rafique and B. Song, *ChemElectroChem*, 2023, **10**, e202200999.
17 Z. J. Baum, L. L. Diaz, T. Konovalova and Q. A. Zhou, *ACS Omega*, 2022, **7**, 32908–32935.
18 D. Strmcnik, P. P. Lopes, B. Genorio, V. R. Stamenkovic and N. M. Markovic, *Nano Energy*, 2016, **29**, 29–36.
19 Y. Zhu, T. Liu, L. Li, S. Song and R. Ding, *Ionics*, 2018, **24**, 1121–1127.
20 N. Krstajić, M. Popović, B. Grgur, M. Vojnović and D. Šepa, *J. Electroanal. Chem.*, 2001, **512**, 16–26.
21 J. L. Weininger and M. W. Breiter, *J. Electrochem. Soc.*, 1964, **111**, 707.
22 X. Yu, J. Zhao, L.-R. Zheng, Y. Tong, M. Zhang, G. Xu, C. Li, J. Ma and G. Shi, *ACS Energy Lett.*, 2018, **3**, 237–244.
23 D. S. Hall, C. Bock and B. R. MacDougall, *J. Electrochem. Soc.*, 2013, **160**, F235–F243.
24 N. Danilovic, R. Subbaraman, D. Strmcnik, K. Chang, A. P. Paulikas, V. R. Stamenkovic and N. M. Markovic, *Angew. Chem., Int. Ed.*, 2012, **51**, 12495–12498.
25 Y. Fang, X. Han, K. Liu, Z. Yuan, Y. Li, S. Tao, Z. Zhang, C. Rao, Q. Fu, G. Peng, X. Yang, D. Wang, Y. Zhang and W. Liao, *Nat. Chem.*, 2026, **18**, 445–456.
26 A. P. Tiwari, J. E. Patterson, M. S. Rahman and W. J. Scheideler, *Adv. Mater. Technol.*, 2025, **10**, e00122.
27 A. P. Tiwari, G. Bae, Y. Yoon, K. Kim, J. Kim, Y.-L. Lee, K.-S. An and S. Jeon, *ACS Sustainable Chem. Eng.*, 2023, **11**, 5229–5237.
28 A. Lavacchi, M. Bellini, E. Berretti, Y. Chen, A. Marchionni, H. A. Miller and F. Vizza, *Curr. Opin. Electrochem.*, 2021, **28**, 100720.
29 Y. X. Chen, A. Lavacchi, H. A. Miller, M. Bevilacqua, J. Filippi, M. Innocenti, A. Marchionni, W. Oberhauser, L. Wang and F. Vizza, *Nat. Commun.*, 2014, **5**, 4036.
30 L. Capozzoli, A. Caprì, V. Baglio, E. Berretti, C. Evangelisti, J. Filippi, I. Gatto, A. Lavacchi, M. Pagliaro and F. Vizza, *J. Power Sources*, 2023, **562**, 232747.
31 M. Bellini, E. Berretti, M. Innocenti, G. Magherini, M. V. Pagliaro, L. Poggini, H. A. Miller, A. Lavacchi and F. Vizza, *Electrochim. Acta*, 2021, **383**, 138338.
32 B. J. O'Neill, D. H. K. Jackson, J. Lee, C. Canlas, P. C. Stair, C. L. Marshall, J. W. Elam, T. F. Kuech, J. A. Dumesic and G. W. Huber, *ACS Catal.*, 2015, **5**, 1804–1825.
33 Z. Gao, M. Dong, G. Wang, P. Sheng, Z. Wu, H. Yang, B. Zhang, G. Wang, J. Wang and Y. Qin, *Angew. Chem., Int. Ed.*, 2015, **54**, 9006–9010.
34 J. Zhang, Y. Pan, D. Feng, L. Cui, S. Zhao, J. Hu, S. Wang and Y. Qin, *Adv. Mater.*, 2023, **35**, 2300902.
35 H. Xu, D. Lin, J. Shi, Z. Lv, X. Zhao, L. Ning, J. Xiao, L. Cui, J. Zhang, J. Yuan, X. Feng, Y. Qin and J. Zhang, *JACS Au*, 2025, **5**, 250–260.
36 https://www.crystallography.net/cod/.
37 B. H. Toby and R. B. Von Dreele, *J. Appl. Crystallogr.*, 2013, **46**, 544–549.
38 F. d'Acapito, G. O. Lepore, A. Puri, A. Laloni, F. La Manna, E. Dettona, A. De Luisa and A. Martin, *J. Synchrotron Radiat.*, 2019, **26**, 551–558.
39 B. Ravel and M. Newville, *J. Synchrotron Radiat.*, 2005, **12**, 537–541.
40 D. A. Shirley, *Phys. Rev. B*, 1972, **5**, 4709–4714.
41 T. Susi, T. Pichler and P. Ayala, *Beilstein J. Nanotechnol.*, 2015, **6**, 177–192.
42 M. C. Biesinger, B. P. Payne, A. P. Grosvenor, L. W. M. Lau, A. R. Gerson, R. St and C. Smart, *Appl. Surf. Sci.*, 2011, **257**, 2717–2730.
43 S. Kumaravel, R. Jayakumar, K. K. Saravanan, V. Niharika, B. Eunice Evangeline, V. Singaram and S. Kundu, *Dalton Trans.*, 2022, **51**, 17454–17465.
44 Y. X. Chen, V. Gombac, T. Montini, A. Lavacchi, J. Filippi, H. A. Miller, P. Fornasiero and F. Vizza, *Green Chem.*, 2018, **20**, 2299–2307.
45 M. Cabán-Acevedo, M. L. Stone, J. R. Schmidt, J. G. Thomas, Q. Ding, H.-C. Chang, M.-L. Tsai, J.-H. He and S. Jin, *Nat. Mater.*, 2015, **14**, 1245–1251.
46 J. Sun, F. Tian, F. Yu, Z. Yang, B. Yu, S. Chen, Z. Ren and H. Zhou, *ACS Catal.*, 2020, **10**, 1511–1519.
47 M. R. Gennero De Chialvo and A. C. Chialvo, *Electrochim. Acta*, 1998, **44**, 841–851.
48 G. N. Derry and Z. Ji-Zhong, *Phys. Rev. B:Condens. Matter Mater. Phys.*, 1989, **39**, 1940–1941.
49 V. Mansfeldova, M. Zlamalova, H. Tarabkova, P. Janda, M. Vorokhta, L. Piliai and L. Kavan, *J. Phys. Chem. C*, 2021, **125**, 1902–1912.
50 M. T. Greiner, M. G. Helander, Z.-B. Wang, W.-M. Tang and Z.-H. Lu, *J. Phys. Chem. C*, 2010, **114**, 19777–19781.
51 H. Prats and K. Chan, *Phys. Chem. Chem. Phys.*, 2021, **23**, 27150–27158.
52 B. Ruqia and S. Choi, *ChemSusChem*, 2018, **11**, 2643–2653.